Chapter 5
Surface Location Error in Milling

No amount of experimentation can ever prove me right; a single experiment can prove me wrong.

- Albert Einstein

In Chapter 4 we described analytical approaches to determining the stability behavior of milling. We showed stability lobe diagrams that identify stable and unstable combinations of spindle speed and axial depth of cut in a graphical format. We also developed time-domain simulations that predict forces and displacements for straight and helical teeth square endmills and helical teeth ball endmills. These simulations could also be employed to determine stability. In this chapter, we presume that stable cutting conditions have been selected and we investigate the influence of forced vibrations on part geometric accuracy. We refer to part errors that occur due to forced vibrations as surface location errors and again apply both analytical frequency-domain and time-domain approaches to their prediction.

5.1 Surface Location Error

As we've seen, the process dynamics can impose significant limitations on milling efficiency due to chatter, or self-excited vibrations that lead to large forces, displacements, and poor surface quality. However, productivity can also be limited by forced vibrations which cause surface location error, or workpiece geometric inaccuracies that result from dynamic displacements of the tool during stable milling [1-14]. Other limiting factors include, for example, machine tool quasi-static positioning errors, thermal errors, contouring errors, and tool wear [15], but we do not address these here.

A visual explanation of the surface location error phenomenon is provided in Fig. 5.1.1. Even under stable cutting conditions, the tool experiences forced/synchronous vibrations which depend on the system frequency response

T.L. Schmitz, K.S. Smith, *Machining Dynamics*, DOI 10.1007/978-0-387-09645-2_5, 173

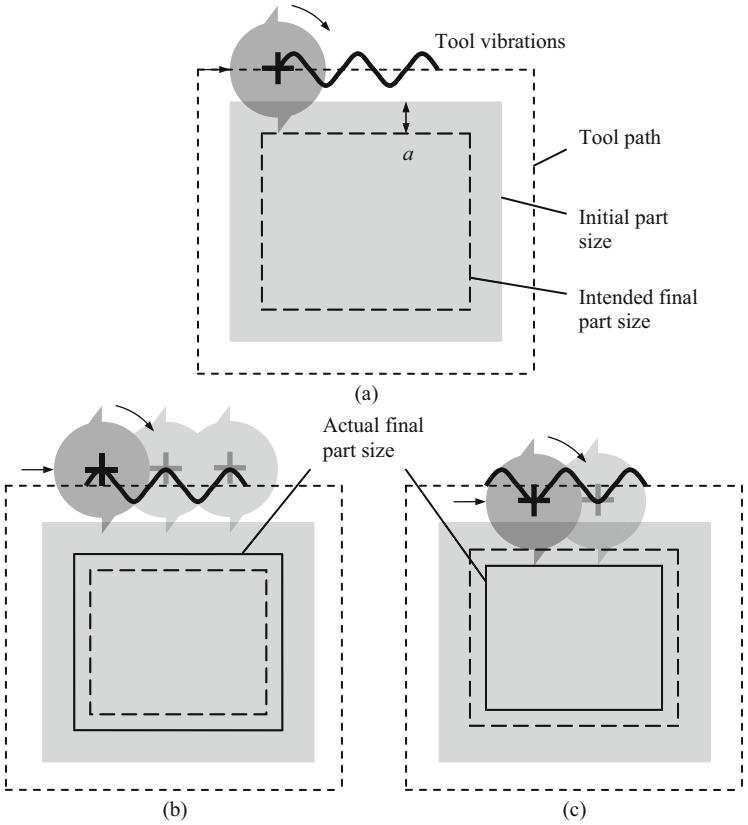

Fig. 5.1.1 Demonstration of surface location error. (a) Intended down milling cut geometry. (b) Undercut example. (c) Overcut example

function, FRF, and excitation frequency (or tooth passing frequency, see Eq. 4.1.14), as well as other process parameters, including the radial and axial depths of cut, feed per tooth, and force model coefficients (although the actual cutting force doesn't inherently obey our selected force model, we do require a model with corresponding coefficients for simulation purposes). In Fig. 5.1.1a, we conveniently assume that the tool vibration follows a sinusoidal profile in the feed direction while peripheral milling a square shape. The position of the tool in its periodic vibration cycle as is exits the down milling cut determines the actual location of the machined surface[1]. In Fig. 5.1.1b, due to the selected tooth passing frequency, the surface is undercut, i.e., less material is removed

[1] This also explains why a vibrating tool can leave a smooth surface. Because the tool vibration is synchronous with rotation, the tool is in the same position each time it creates the new surface.

than commanded. In this case, the tool vibration is away from the intended surface at each instant that a tooth is exiting the cut (only these cutter angles are shown and the lateral scale is greatly exaggerated). Figure 5.1.1c represents the overcut condition where more material is removed than commanded. Now the tool vibration is toward the intended surface when the tool is exiting the cut. Analogous representations could be provided for up milling, except we are interested in the tool location as it enters the cut.

The source of the surface location error behavior is the variation of the machine-spindle-holder-tool, and potentially the workpiece-fixture, FRF magnitude and phase with forcing frequency (as shown in Fig. 2.2.3, for example). Due to the change in phase with tooth passing frequency (spindle speed), the time lag between the force and vibration varies. Therefore, the location of the cutter in its vibration cycle when leaving the surface depends on the selected spindle speed. The dependence of surface location error on the phase lag between the forcing function and displacement causes significant variation near the natural frequency (considering a single degree of freedom system for simplicity) because for the lowly damped tool point FRFs typically observed in practice, the phase changes rapidly in this frequency range. To explore this behavior, we first describe a frequency-domain solution to surface location error and then demonstrate the spindle speed dependence with numerical examples.

IN A NUTSHELL The concept of surface location error may be surprising to some readers. In CNC programming packages, the tool is modeled as a cylinder (or perhaps a cylinder with a spherical end), the workpiece is modeled as a prismatic solid, and the workpiece is created by the relative motion of the cylinder with respect to the solid. However, the tool is not a cylinder. It is a collection of cutting edges that rotate together.

It is obvious to many that the tool and workpiece are not rigid. This is certainly one of the reasons for making a roughing pass followed by a finishing pass. This intuition reveals the static surface location error. However, actual surface generation is more complicated than a static deflection. The variable cutting force, even in stable machining, causes the tool to vibrate. The surface location is controlled by the position of the tool in its cycle of vibration at the time that a tooth is in a position to generate the final surface. The tool may exhibit large vibrations, yet still produce an accurately located surface. Alternately, these large vibrations may produce significant errors in the surface location.

By analogy, we might imagine that the vibrating tool is like a swing on a playground. The surface generation is like the moment of contact between the pusher and the swing. The pusher can stand far behind the swing and push as the swing reaches its peak displacement (poorly located surface) or the pusher

may stand to the side and push the swing as it passes through its equilibrium position (perfectly located surface).

Of course, the cutting operation is more complicated. Naturally, the surface location error is spindle speed dependant. The spindle speed sets the frequency of the force exciting the vibration and, therefore, defines the resulting displacement according to the frequency response function. In addition, if the cutter teeth are helical, then different levels of the surface are generated at different instants in time. The surface location error along a line parallel to the tool's rotation axis, therefore, varies from the tip of the tool to the full axial depth of cut.

5.2 Frequency-Domain Solution

In chapter 4 we described the average tooth angle [16] and Fourier series [17] approaches to stability behavior prediction in milling. Both were frequency-domain methods that relied on knowledge of the FRF and force model coefficients. To complement these analytical tools, we now describe a frequency-domain solution to surface location error [18]. Together, these provide a comprehensive picture of the role of milling dynamics in process productivity.

In order to determine surface location error using a frequency-domain (or steady-state) approach, we make two basic assertions. First, although vibrations of the cutter occur in both the x and y directions, the y direction vibrations dominate the final surface location for an x direction feed. Second, regeneration can be neglected in stable machining. Based on these assumptions, the concept is to: 1) express the y direction cutting force in the frequency-domain, $F_y(\omega)$ using a Fourier series; 2) determine the frequency-domain y displacement, $Y(\omega)$, by multiplying $F_y(\omega)$ by the machine-spindle-holder-tool direct FRF (measured or modeled at the tool point) in the y direction, $\frac{Y(\omega)}{F_y(\omega)}$; and 3) inverse Fourier transform this result and sample at the cut entry (up milling) or exit (down milling) to find the surface location error. Note that, unlike time-domain simulation, the tool point FRF can be used directly without the requirement for a modal fit in this approach.

5.2.1 Fourier Force Model

If we apply the cutting force model provided in Eq. 5.2.1, which relates the tangential, F_t, and normal, F_n, cutting force components to the axial depth of cut, b, and chip thickness, h, $F_y(\phi)$ can be expressed as shown in Eq. 5.2.2. In this equation, the summations account for all possible teeth within the cut, a circular tool path is assumed, f_t is the feed per tooth, and $g(\phi_i)$ is the switching function previously defined in Eq. 4.3.10. Also, the angle of each tooth, i (N_t total), at any

instant in time is $\phi_i = \omega t + \frac{2\pi}{N_t}(i-1)$ (rad), where ω is the spindle rotating frequency (in rad/s).

$$\begin{aligned} F_t(\phi) &= k_t b h(\phi) + k_{te} b \\ F_n(\phi) &= k_n b h(\phi) + k_{ne} b \end{aligned} \tag{5.2.1}$$

$$F_y(\phi) = -b \begin{bmatrix} \frac{-k_t f_t}{2} \sum_{i=1}^{N_t} g(\phi_i)(1-\cos(2\phi_i)) + \frac{k_n f_t}{2} \sum_{i=1}^{N_t} g(\phi_i)\sin(2\phi_i) - \\ k_{te} \sum_{i=1}^{N_t} g(\phi_i)\sin(\phi_i) + k_{ne} \sum_{i=1}^{N_t} g(\phi_i)\cos(\phi_i) \end{bmatrix} \tag{5.2.2}$$

The equivalent Fourier series for the y direction cutting force can be written once the Fourier coefficients, a_n and b_n, are determined.

$$F_y(\phi) = \sum_{i=1}^{N_t} \left(a_0 + \sum_{n=1}^{\infty} (a_n \cos(n\phi_i) + b_n \sin(n\phi_i)) \right)$$

The a_0 term, for example, can be found using Eq. 5.2.3, where the integral for a full revolution of the selected tooth may be divided into three parts. The three subsequent integrals are delineated by ϕ_1, which represents the cut entry angle in down milling or cut exit angle in up milling, and π rad, which defines the maximum angle that a tooth can be engaged in the cut (if ϕ is defined positive in a clockwise sense from the positive y axis). See Fig. 5.2.1. Considering a down milling cut, for example, only the middle of the three integrals in Eq. 5.2.3 is nonzero due to the switching function embedded in $F_y(\phi)$. Performing the relevant integration for down milling yields Eq. 5.2.4. For up milling, only the first integral in Eq. 5.2.3 is nonzero and the integration limits become zero to ϕ_1 in Eq. 5.2.4.

$$a_0 = \frac{1}{2\pi} \int_0^{2\pi} F_y(\phi) d\phi = \frac{1}{2\pi} \left[\int_0^{\phi_1} F_y(\phi) d\phi + \int_{\phi_1}^{\pi} F_y(\phi) d\phi + \int_{\pi}^{2\pi} F_y(\phi) d\phi \right] \tag{5.2.3}$$

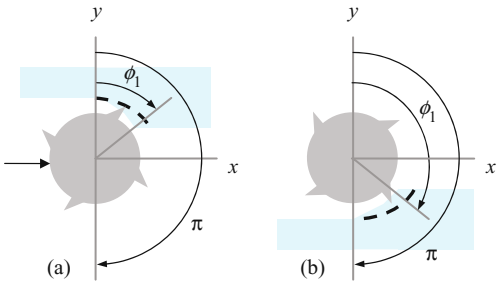

Fig. 5.2.1 Angles for Fourier series integrals. (a) Up milling. (b) Down milling

$$a_0 = -\frac{bN_t}{2\pi}\left[-\frac{k_t f_t \phi}{2} + \frac{k_t f_t}{4}\sin 2\phi - \frac{k_n f_t}{4}\cos 2\phi + k_{te}\cos\phi + k_{ne}\sin\phi\right]_{\phi_1}^{\pi} \quad (5.2.4)$$

The a_n coefficients are computed using Eq. 5.2.5 and the b_n coefficients using Eq. 5.2.6. Again, the integrals can be partitioned using ϕ_1 and π as shown in Eq. 5.2.3. Closed-form equations for the $n = 3, 4, 5, \ldots$ coefficients are determined by observing the recursive patterns after integration. See Appendix C.

$$a_n = \frac{1}{\pi}\int_0^{2\pi} F_y(\phi)\cos(n\phi)d\phi \quad (5.2.5)$$

$$b_n = \frac{1}{\pi}\int_0^{2\pi} F_y(\phi)\sin(n\phi)d\phi \quad (5.2.6)$$

To accurately represent milling forces, however, it is also necessary to account for the influence of the teeth helix angle, γ. This can be accomplished by sectioning the tool into A axial slices. Each slice is assumed to have a zero helix angle and the slices are rotated relative to one another by the angle $\chi = \frac{2db\tan(\gamma)}{d}$ (rad), where db is the slice height and d is the cutter diameter (see Fig. 4.5.3). The Fourier series is now written as $F_y(\phi) = \sum_{j=1}^{A}\sum_{i=1}^{N_t}\left(a_0 + \sum_{n=1}^{\infty}(a_n\cos(n\phi_i) + b_n\sin(n\phi_i))\right)$, where $\phi_i = \omega t + \frac{2\pi}{N_t}(i-1) - \chi(j-1)$. Naturally, a larger number of slices improves the force fidelity.

Example 5.2.1: Fourier series force dependence on number of coefficients As expected, the accuracy of the Fourier series force depends on the number, n, of coefficients included in the series. Figure 5.2.2 shows a comparison of the y direction force determined by time-domain simulation and its Fourier series for $n = 5$ and $n = 50$. The cutting conditions are: up milling, 25% radial immersion, $N_t = 4$, $d = 19$ mm, $\gamma = 30$ deg, $b = 1$ mm, $f_t = 0.1$ mm/tooth, $k_t = 700$ N/mm^2, $k_n = 210$ N/mm^2, $k_{te} = k_{ne} = 0$ N/mm, and $\omega = 300\pi$ rad/s (i.e., the spindle speed, Ω, is 9000 rev/min, or rpm). Figure 5.2.2 was generated using the MATLAB® program p_5_2_1_1.m included on the companion CD. The MATLAB® function `eval`, used to evaluate strings, was implemented to enable an arbitrary number of Fourier coefficients to be computed without requiring significant reprogramming.

Example 5.2.2: Frequency-domain surface location error calculations The four steps for frequency-domain surface location error prediction, namely:

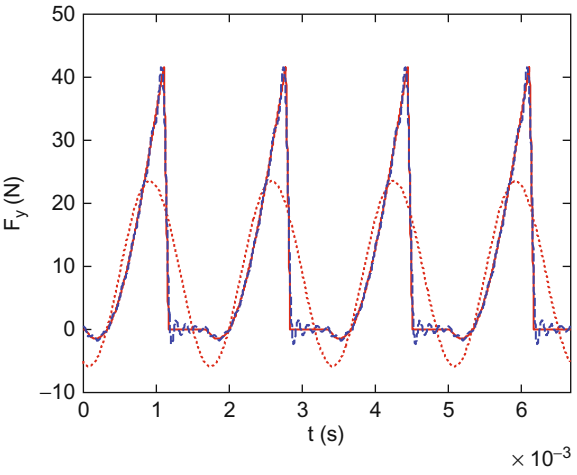

Fig. 5.2.2 Force reconstruction using time-domain (solid line) and Fourier series (dotted line: $n = 5$; dashed line: $n = 50$). Additional coefficients increase the force fidelity

- using a Fourier series to determine $F_y(t)$ and applying the discrete Fourier transform to obtain $F_y(\omega)$;
- calculating the frequency-domain y displacement using $Y(\omega) = \frac{Y(\omega)}{F_y(\omega)} F_y(\omega)$, where $\frac{Y(\omega)}{F_y(\omega)}$ is the y direction machine-spindle-holder-tool direct FRF (at the tool point);
- inverse Fourier transforming $Y(\omega)$ to obtain $y(t)$; and
- sampling it at the cut entry (for up milling) or exit (for down milling), are carried out in p_5_2_2_1.m. The function, p_5_2_2_2.m, called from within p_5_2_2_1.m, actually completes the individual surface location error computations.

To compare the surface location error (SLE) in up and down milling, simulations were completed for the following conditions: 50% radial immersion (up and down milling) at spindle speeds from 6900 rpm to 7800 rpm, $N_t = 4$, $\gamma = 30$ deg, $d = 12.7$ mm diameter, $f_t = 0.1$ mm/tooth, $b = 1$ mm, $k_t = 700$ N/mm^2, $k_n = 210$ N/mm^2, $k_{te} = k_{ne} = 0$ N/mm, symmetric structural dynamics with a stiffness of 1×10^7 N/m, 1% damping (i.e., a damping ratio, ζ, of 0.01), and 500 Hz natural frequency. The results are displayed in Fig. 5.2.3, where 50 terms were used in the Fourier series force model. It is seen that the surface location error yields an overcut surface in both instances. For up milling, the positive SLE means that cutter is radially deeper into the cut than commanded when creating the final surface. Similarly, for down milling, the negative SLE indicates that the cutter is farther into the cut than desired.

Because the frequency-domain surface location error simulation neglects regeneration, stable conditions are predicted in all instances (i.e., only forced vibrations are considered). Therefore, these calculations must be accompanied by the appropriate stability lobe diagram to select stable machining parameters. The Fourier series approach stability lobe diagram corresponding to the

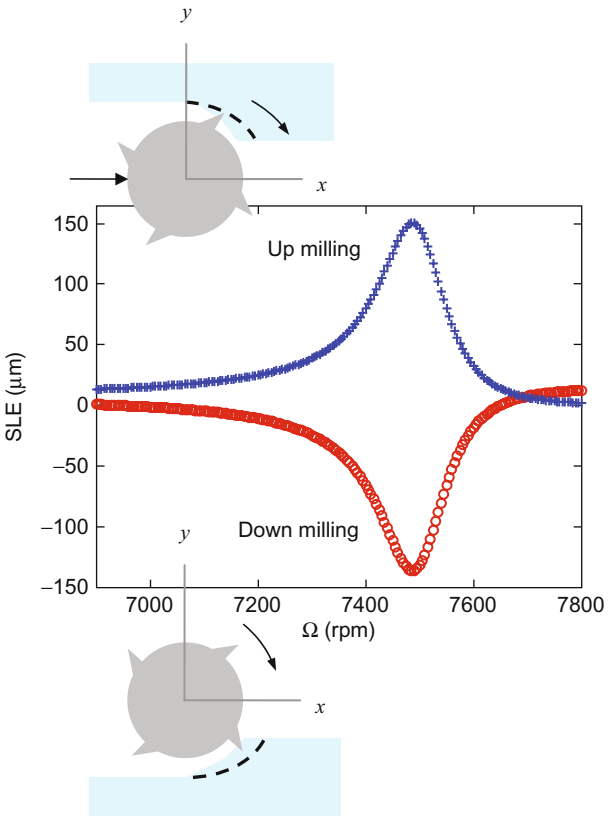

Fig. 5.2.3 Surface location error (SLE) for Ex. 5.2.2. Both up and down milling lead to an overcut condition

selected up milling scenario is provided in Fig. 5.2.4. The stability lobe diagram for 50% radial immersion down milling is nearly identical and is not shown. The test range for the surface location error simulations is indicated by the solid line. It is verified that the selected cutting conditions for Fig. 5.2.3 are in the stable zone. Figure 5.2.4 was generated using the MATLAB® program p_5_2_2_3.m.

To compare surface location error trends over a broader range, calculations were completed using the same system under 50% radial immersion up milling for spindle speeds from 6900 rpm to 7700 rpm and axial depths from 0.5 mm to 5 mm. See the dotted rectangle in Fig. 5.2.4. The surface location error contours (lines of constant error) are provided in Fig. 5.2.5, where 50 terms were again used for the Fourier series force. An interesting aspect of this figure is the high sensitivity of surface location error to spindle speeds near 7500 rpm. Using Eq. 4.3.7, we see that the best speeds for increasing axial depth of cut without chatter are:

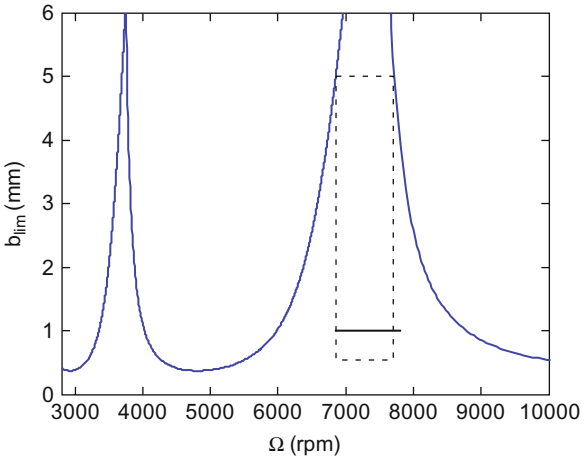

Fig. 5.2.4 Stability lobe diagram for Ex. 5.2.2 (50% radial immersion up milling). Two test ranges are also identified: (solid line) 6900 rpm to 7800 rpm at 1 mm axial depth; and (dotted line rectangle) 6900 rpm to 7700 rpm with axial depths from 0.5 mm to 5 mm

$$\Omega_{best} = \frac{f_n \cdot 60}{(N+1) \cdot N_t} = \frac{500 \cdot 60}{(N+1) \cdot 4} = \frac{7500}{(N+1)}.$$

For the right-most ($N = 0$) lobe highlighted by the rectangular simulation range in Fig. 5.2.4, the best speed is therefore in the high slope surface location error range. This high slope indicates that small errors in our knowledge of the system dynamics or spindle speed could lead to significant changes in the predicted error and affect our ability to compensate by tool path adjustments, for example. We also see that the error tends to increase with axial depth. This result is expected given that the force magnitude, and consequently the

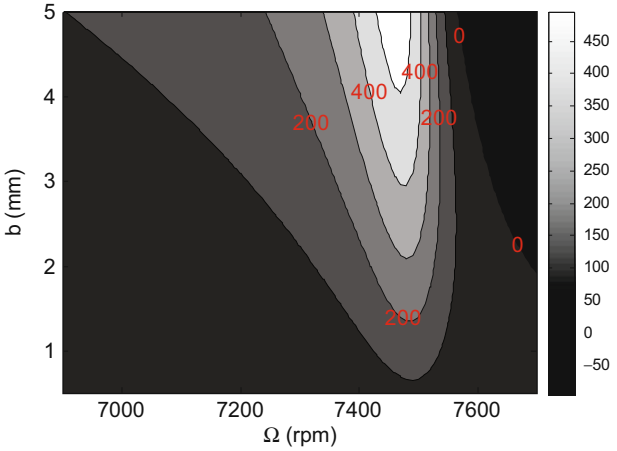

Fig. 5.2.5 Surface location error contours for rectangular stable zone identified in Fig. 5.2.4. High sensitivity of the error to spindle speed is observed near 7500 rpm, the traditional best speed for increased chatter-free axial depth of cut

vibration level, scales with axial depth. While these results do not preclude the use of the best speeds equation to select a preferred spindle speed, it does demonstrate that combining consideration of surface location error with stability may lead to a slightly different spindle speed choice to balance the two requirements. This is explored further at the end of this section. Figure 5.2.5 was generated using the MATLAB® program p_5_2_2_4.m.

A natural question to ask is if this same variation in surface location error also occurs in higher N value stability lobes. To answer this question, let's complete simulations for the spindle speed range from 2000 rpm to 10000 rpm. This span encompasses the first three best speeds ($N = 0$, 1, and 2) at 7500 rpm, 3750 rpm, and 2500 rpm. Using a 25% radial immersion to raise the critical stability limit (the depth at which the cut is stable for all spindle speeds) and enable an axial depth of 0.75 mm, but maintaining consistency in all other conditions with respect to Fig. 5.2.5, produces the error variation displayed in Fig. 5.2.6 (p_5_2_2_5.m). We see that the surface location error shows sensitivity to spindle speed at each of the best speeds.

IN A NUTSHELL It can be seen that over broad segments of the spindle speed range, the surface location error is quite small. However, there are also narrow bands in which the surface location error is large or changes rapidly from large negative to large positive values, for example. Unfortunately, these sections of extreme speed sensitivity are located within the stable zones of the stability lobe diagram. It is for this reason that the combined ability to choose stable cutting parameters as well as predict the surface location error is so important.

As noted in Section 5.1, it is the change in phase with frequency that varies the time lag between the force and vibration and causes the surface location error dependence on spindle speed. Further, the variation in phase with tooth passing

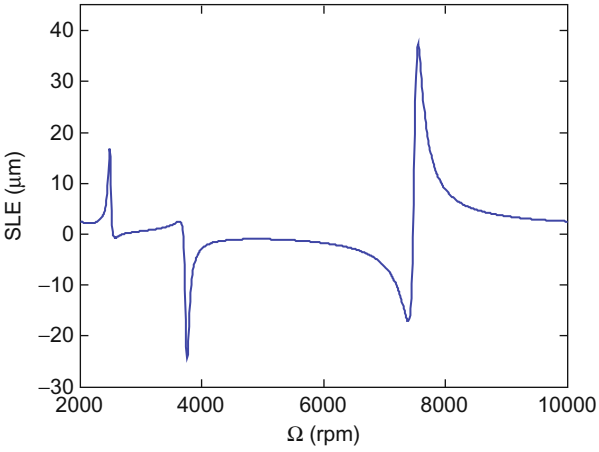

Fig. 5.2.6 Variation in surface location error from 2000 rpm to 10000 rpm for the system described in Ex. 5.2.2. The up milling radial immersion is 25% and the axial depth is 0.75 mm. The behavior is periodic with error sensitivity near the best speeds identified in Eq. 4.3.7

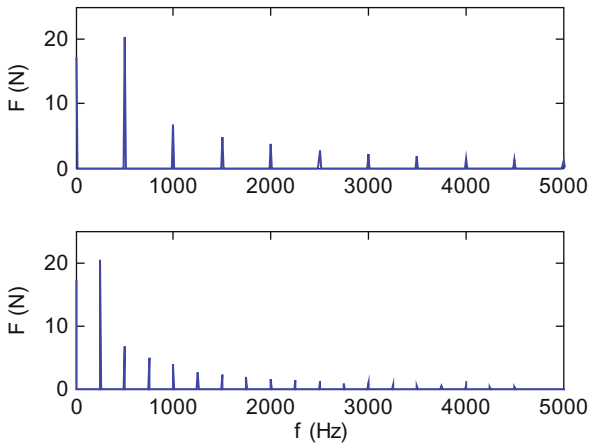

Fig. 5.2.7 Force spectrum for 7500 rpm (top) and 3750 rpm (bottom)

frequency (zero to -180 deg for a single degree of freedom system) is strongest near the natural frequency. The repetitive behavior observed in Fig. 5.2.6 occurs as increasing harmonics of the fundamental tooth passing frequency excite the system resonance. Figure 5.2.7 shows the spectra of the *y* direction cutting force for 7500 rpm and 3750 rpm (p_5_2_2_6.m). At 7500 rpm (top), the first harmonic, or fundamental peak, is coincident with the 500 Hz natural frequency. At 3750 rpm, (bottom) the first harmonic occurs at 250 Hz, but the second harmonic now matches the natural frequency. Similarly, the third harmonic excites resonance at 2500 rpm (not shown). The surface location error magnitude decreases with each increasing N value because the energy in the subsequent harmonics reduces. Figure 5.2.8 is included to demonstrate this phenomenon pictorially.

As a final activity before considering the effect of the helix angle on surface location error, let's investigate the influence of radial depth of cut. We'll use the same dynamic system with a spindle speed range of 6900 rpm to 7800 rpm and vary the radial engagement for down milling from 50% to 20% in decrements of 10%. The corresponding starting angles are {90, 101.5, 113.6, and 126.9} deg, respectively, as calculated using Eq. 4.1.5 and the exit angle is always 180 deg for down milling based on the circular tool path approximation. Let's select an axial depth below the 50% radial immersion critical stability limit. We can see from Fig. 5.2.4 that $b = 0.35$ mm ensures stable conditions for any spindle speed so we'll apply that value (although Fig. 5.2.4 is for up milling, the stability limit is similar for down milling at the same radial immersion in this case). The results, which were obtained using p_5_2_2_7.m, are provided in Fig. 5.2.9. We see that the transition from overcutting (negative error for down milling) to undercutting (positive error for down milling) near the $N = 0$ best spindle speed shifts to the left as the radial

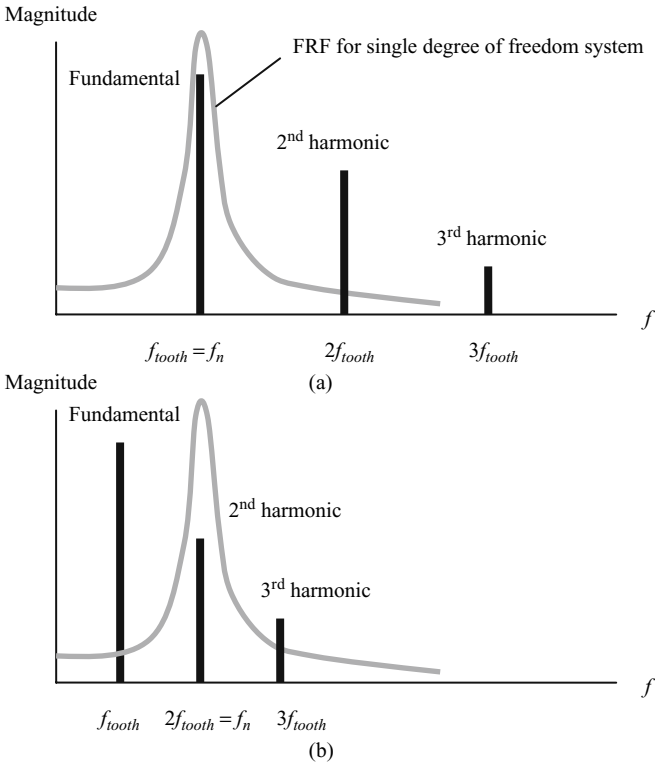

Fig. 5.2.8 Description of periodic surface location error variation. (a) The tooth passing frequency is coincident with the natural frequency (resonant force vibrations) for the $N = 0$ best spindle speed. (b) The second harmonic is located at resonance for the $N = 1$ best spindle speed

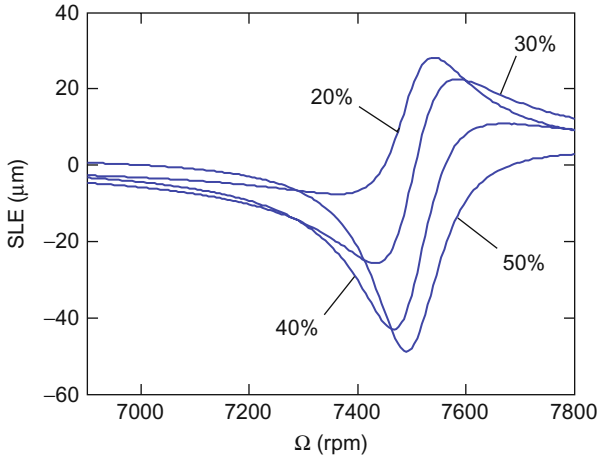

Fig. 5.2.9 Variation in surface location error with radial depth of cut. The four curves represent percent radial immersion cases of 50% to 20% down milling with a constant axial depth of 0.35 mm. The system dynamics are the same as were defined in Ex. 5.2.2

immersion is reduced. Also, the shape of the error profile changes and the peak-to-peak magnitude decreases. The latter occurs because the force level reduces with smaller radial depth of cut.

5.2.2 Variation in Surface Location Error with Axial Location

As discussed in Section 4.5, the effect of the helical cutting edge geometry is that the full length of the cutting edge does not enter (or exit) the cut at the same instant. The edge nearest the free end of the tool enters first and there is an increasing delay of the cut entry (and exit) for points on the edge that are farther from the free end (toward the spindle). The helical square endmill geometry considered here is shown in Fig. 5.2.10.

Due to the entry delay for up milling and exit delay for down milling, the surface location error varies with axial location (z direction) along the helical cutting edge length. Effectively, this occurs because the surface location is determined by the time dependent y vibration, but all points along the surface (in the z direction) are not generated simultaneously. Relative to the free end of the cutter, the angular delay along the tool axis is $\chi = \frac{2|z|\tan(\gamma)}{d}$ (rad), where $|z|$ is the absolute value of the distance from the end. The corresponding time delay is $\frac{\chi}{\frac{\Omega 2\pi}{60}}(s)$, where Ω is the spindle speed in rpm. The surface along the cutter axis (from the free end toward the spindle) is therefore produced at progressively later points in time while the cutter vibration state varies continuously. This leads to a periodic variation in the surface location error with the z value, as shown in [14].

We can use the MATLAB® program p_5_2_2_8.m to investigate this behavior. Similar to the time-domain simulations in Sections 4.5 and 4.6, the tool is discretized into axial slices. The angular delay with z location is handled by changing the times at which the $y(t)$ vector is sampled to determine surface location error. For axial slices not at the tool point, the time vector is sampled later than the cut entry (up milling) or exit (down milling) by `dX*(cnt-1)/(omega/60*2*pi)`, where `cnt = 1, 2, 3...` is the index of the current axial slice (equal to 1 at the tool

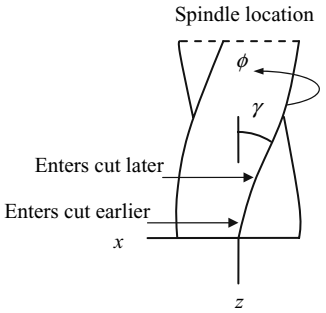

Fig. 5.2.10 The helical endmill geometry causes the cutting edge to enter and exit the cut at later instants in time when moving from its free end toward the spindle (the feed direction is to the left for this figure)

point), the delay angle per slice is `dX = 2*db*tan(gamma*pi/180)/d` (rad), `db` is the slice width in the z direction, `gamma` is the helix angle (deg), and `d` is the tool diameter. Figure 5.2.11 shows the results for 50% radial immersion up milling with the same specifications provided previously. The spindle speed is 7500 rpm and the axial depth of cut is 12 mm; the stability of this cut was verified using p_5_2_2_3.m. Clearly, the surface location error is strongly dependent on the axial location for this example, where the $|z| = 0$ location corresponds to the tool's free end and the orientation is the same as shown in Fig. 5.2.10. We should state explicitly here that all previous figures reported results for the error only at the free end of the cutting tool. For comparison purposes, p_5_2_2_8.m was used to calculate the surface location error for $b = 6$ mm at 3750 rpm, the $N = 1$ best speed from Fig. 5.2.4. This result is provided in Fig. 5.2.12. We see that the general profile is maintained relative to Fig. 5.2.11, although the error magnitude is decreased (the smaller axial depth gives smaller force and deflection) and the spatial period (in z) is reduced.

Let's explore what happens to surface location error and its axial variation if we select the axial depth for constant cutting force, as described in Section 4.5. For the selected tool, the constant cutting force axial depth is:

$$b = \frac{d \cdot \phi_p}{2\tan(\gamma)} = \frac{12.7 \cdot 90\frac{\pi}{180}}{2\tan(30)} = 17.3\,\text{mm}.$$

Unfortunately, this axial depth is unstable for the given FRF and force model, even at the $N = 0$ best speed of 7500 rpm. If the helix angle is increased to 45 deg, however, the constant force depth becomes 10.0 mm, which is stable at 7500 rpm. In this case, the constant force eliminates the surface location error variation with axial depth due to the time invariance of the vibration, i.e., constant force yields constant deflection (after the initial transients have

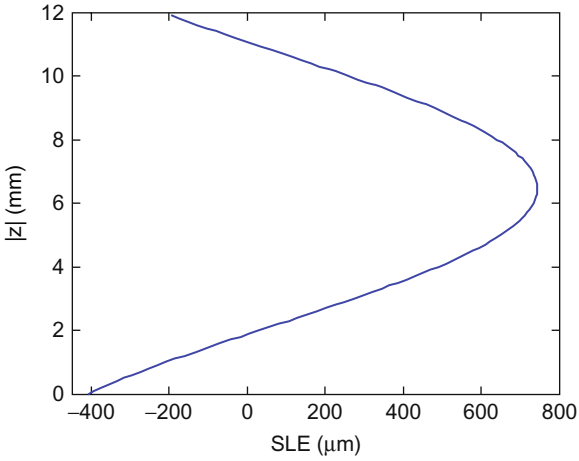

Fig. 5.2.11 Surface location error variation with axial location for $b = 12$ mm, $\Omega = 7500$ rpm, and $\gamma = 30$ deg (helix angle). The $|z| = 0$ position corresponds to the tool's free end (see Fig. 5.2.10)

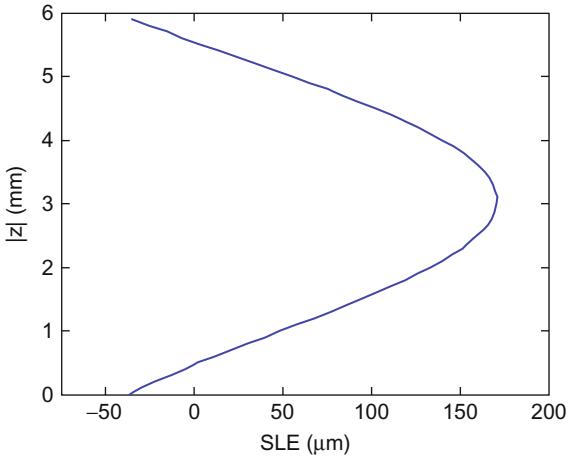

Fig. 5.2.12 Surface location error variation with axial location for $b = 6$ mm, $\Omega = 3750$ rpm, and $\gamma = 30$ deg

decayed) so the time at which the cutter enters or exits the cut does not change the error. We must realize that the resulting surface location error still is not zero, even for the constant force condition. The error is simply determined from the ratio of the force to the stiffness, where $k = 1 \times 10^7$ N/m for this example. The MATLAB® program p_5_2_2_9.m was used to generate Fig. 5.2.13, which displays the y direction force, $F_y = 284$ N at steady state, and corresponding deflection, $y = \frac{284}{1 \times 10^7} = 2.8 \times 10^{-5}$ m $= 28$ μm. For the selected up milling 50% radial immersion cut, this gives an overcut surface. However, the error is small

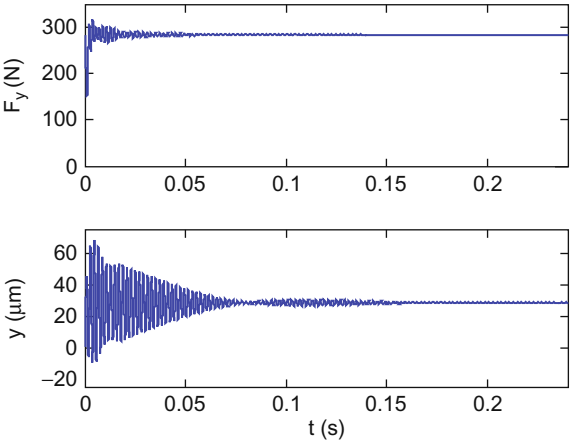

Fig. 5.2.13 Constant y direction cutting force and displacement when $b = 10.0$ mm for a helix angle of 45 deg on the four tooth, 12.7 mm diameter endmill

relative to the 12 mm axial depth, non-constant force results shown in Fig. 5.2.11.

IN A NUTSHELL The helix of the tool allows the surface location error to vary along the axis of an endmill. For this reason, a perfectly ground, exactly centered, and correctly balanced endmill that is rotating in a spindle with no error motions may still produce a non-straight sidewall during peripheral milling. The error along the wall that is parallel to the axis of the tool is a record of the tool's dynamic displacement as it rotates because different levels of the wall (bottom to top) are created at successive instants in time during the tool's rotation.

5.2.3 Combining Stability and Surface Location Error in a Single Diagram

As a final activity in this section, let's combine the stability and surface location error data in a single diagram. We'll consider the following conditions: 50% radial immersion up milling at spindle speeds from 2800 rpm to 10000 rpm, $N_t = 4$, $\gamma = 30$ deg, $d = 12.7$ mm diameter, $f_t = 0.1$ mm/

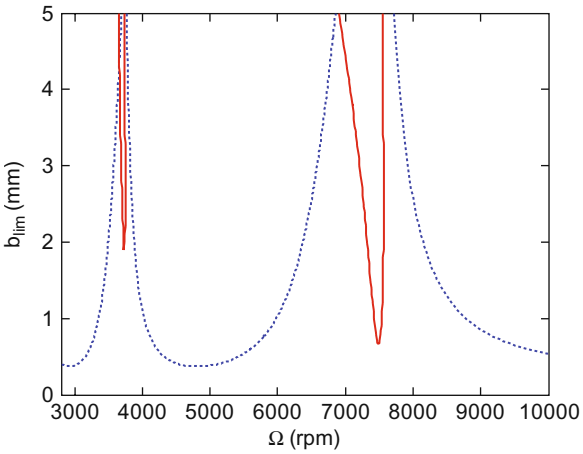

Fig. 5.2.14 Stability (dotted line) and surface location error (solid line) information combined in a single "super" diagram. The solid contour lines identify the {spindle speed, axial depth} combinations where the error level is 100 μm. The simulation parameters are: 50% radial immersion up milling, $N_t = 4$, $\gamma = 30$ deg, $d = 12.7$ mm diameter, $f_t = 0.1$ mm/tooth, $k_t = 700$ N/mm^2, $k_n = 210$ N/mm^2, $k_{te} = k_{ne} = 0$ N/mm, and symmetric structural dynamics with a stiffness of 1x10^7 N/m, 1% damping, and 500 Hz natural frequency

tooth, b = 0.4 mm to 5 mm (for the surface location error calculations), k_t = 700 N/mm^2, k_n = 210 N/mm^2, k_{te} = k_{ne} = 0 N/mm, and symmetric structural dynamics with a stiffness of 1×10^7 N/m, 1% damping, and 500 Hz natural frequency. The results are displayed in Fig. 5.2.14, where 15 terms were used in the Fourier series force model[2]. The MATLAB® program p_5_2_2_10.m was executed to generate the figure, which displays the stability boundary (dotted line) in addition to surface location error contours (solid lines) at a constant error level of 100 μm; note that the surface location error was calculated at the free end of the tool for this example. The error level is larger within the contours similar to Fig. 5.2.5. This "super" diagram shows that a portion of the stable zone (inside the error contours) is inaccessible if the user desires the surface location error to be less than 100 μm. The information provided in Fig. 5.2.14 could be used at the process planning stage, for example, to select machining conditions that satisfy both stability and accuracy requirements.

5.3 Cycloidal Tool Path Time-Domain Simulation

Similar to Sections 4.4 and 4.5., we now detail a time-domain milling simulation based on the 'Regenerative Force, Dynamic Deflection Model' described by Smith and Tlusty [6]. The simulation includes the contribution of the tool vibrations to the instantaneous chip thickness and provides predictions for both force and deflection in the x (feed) and y directions. Vibrations along the tool axis, or z direction, are not considered. We also model the cycloidal motion of the cutter teeth, rather than assuming a circular tool path. Other instances of cycloidal tool path simulations from the literature are provided in [19–21], for example. Our approach [22] is similar in nature to that described in [21].

We begin the milling simulation by first defining the cutting parameters, including spindle speed, Ω, feed per tooth, f_t, radial and axial depths of cut, a and b, respectively, and the number of teeth, N_t. We then describe the system dynamics using the modal mass, m, damping, c, and stiffness, k, values for any number of modes in the x (feed) and y directions. As detailed in Section 2.5, these values are typically obtained from impact tests followed by a modal fitting procedure, such as the peak picking method.

We determine the forces and deflections by numerical integration over small steps in time, $dt = \frac{60}{SR \cdot \Omega}$ (sec), where SR is the number of steps per cutter revolution and Ω is expressed in rpm. In each time step, we rotate the cutter

[2] In general, it is not necessary to use a large number of terms to represent the force. It is usually only necessary that the first few harmonics be characterized since higher order harmonics often have little impact on the system behavior.

by an angle, $d\phi = \frac{360}{SR}$ (deg). We then calculate the current nominal coordinates of each tooth on the cutter (Cx_j, Cy_j) according to Eq. 5.3.1, where r is the cutter radius, ϕ_j is the tooth angle, j is the tooth number which varies from 1 to N_t, $df = \frac{N_t f_t}{SR}$ is the incremental feed during the time step dt, and x_{tool} and y_{tool} are the tool center coordinates determined in the previous time step (set equal to zero initially).

$$\begin{aligned} Cx_j &= r\sin\phi_j + df + x_{tool} \\ Cy_j &= r\cos\phi_j + y_{tool} \end{aligned} \tag{5.3.1}$$

In order to calculate the instantaneous chip thickness at each time step, we compare the (Cx_j, Cy_j) coordinates of the current tooth (i.e., point **C** in Fig. 5.3.1) to the surface coordinates recorded during the prior tooth passage at the same angular orientation. However, because we are not applying the circular tool path assumption, it is not required that a data point exist at this angle from the prior pass. Therefore, we must complete a search to determine the two points from the previous tooth passage which bound this angle; we refer to these points as **A** and **B** in Fig. 5.3.1. We then carry out linear interpolation between points **A** and **B** to determine point **D**, which lies on the line between point **C** and the cutter origin [23]. The coordinates of point D, (Dx_j, Dy_j), are given in Eq. 5.3.2:

$$\begin{aligned} Dx_j &= \frac{\tan(\phi_j)\cdot Ax_j C^* - \tan(\phi_j)\cdot Ay_j + \tan(\phi_j)\cdot Cy_j - Cx_j}{\tan(\phi_j)\cdot C^* - 1} \\ Dy_j &= Ay_j - Ax_j C^* + Dx_j C^* \end{aligned}, \tag{5.3.2}$$

where $C^* = \frac{Ay_j - By_j}{Ax_j - Bx_j}$. We include the nonlinearity that is exhibited when the vibration amplitude is large enough that a tooth leaves the cut by setting the chip thickness, h_j, equal to zero if:

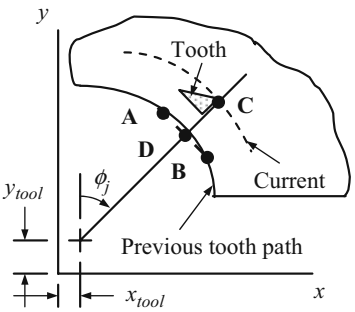

Fig. 5.3.1 Determination of instantaneous chip thickness by linear interpolation for cycloidal tool path

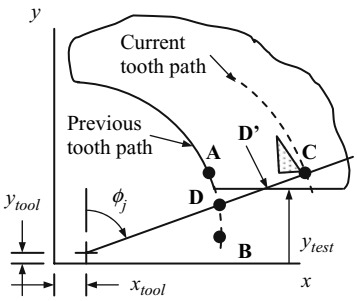

Fig. 5.3.2 Reduced instantaneous chip thickness at cut exit in up milling

$$\sqrt{\left(Cx_j - x_{tool}\right)^2 + \left(Cy_j - y_{tool}\right)^2} < \sqrt{\left(Dx_j - x_{tool}\right)^2 + \left(Dy_j - y_{tool}\right)^2}. \quad (5.3.3)$$

We must also query two other conditions for the chip thickness calculation. First, we must determine if the current tooth is bounded by the specified radial immersion. Second, we must verify that the chip thickness has not been reduced during cut entry for down milling or cut exit for up milling. The chip thickness reduction that occurs at the cut exit for up milling, for example, is exhibited in Fig. 5.3.2.

To determine if the current tooth is bounded by the selected radial depth of cut (i.e., engaged in the cut), we use the value y_{test}, which gives the y direction coordinate of the desired surface as shown in Fig. 5.3.2. For up milling with less than or equal to 50% radial immersion, cutting occurs if Cy_j is greater than y_{test}. This situation is depicted in Fig. 5.3.2. If the up milling radial immersion is greater than 50%, then Dy_j must be greater than y_{test} if cutting is to occur (note that y_{test} is negative in this case). For down milling, Cy_j must be less than y_{test} if the radial immersion is less than or equal to 50% and cutting is to take place (y_{test} is again negative). If the radial immersion is greater than 50%, it is required that Dy_j be less than y_{test} if cutting is to occur. In each case, provided the chip thickness is not reduced at the cut exit (up milling) or entry (down milling), as shown in Fig. 5.3.2, and the tooth has not vibrated out of the cut (Eq. 5.3.3), then h_j is calculated according to Eq. 5.3.4:

$$h_j = \sqrt{\left(Cx_j - Dx_j\right)^2 + \left(Cy_j - Dy_j\right)^2}. \quad (5.3.4)$$

To check if the chip thickness reduction condition is met, we again compare the tooth coordinates to y_{test}. The thickness reduction occurs if the following circumstances are satisfied: 1) up milling, less than or equal to 50% radial immersion: Dy_j is less than y_{test}; 2) up milling, greater than 50% radial immersion: Cy_j is less than y_{test}; 3) down milling, less than or equal to 50% radial immersion: Dy_j is greater than y_{test}; and 4) down milling, greater than 50% radial immersion: Cy_j is greater than y_{test}. In these cases, we can no longer use

Eq. 5.3.4 to compute the instantaneous chip thickness. Rather, we must consider point $\mathbf{D}'$ identified in Fig. 5.3.2. The coordinates of this point, (Dx'_j, Dy'_j), are provided in Eq. 5.3.5.

$$\begin{aligned} Dx'_j &= (y_{test} - y_{tool}) \tan \phi_j + x_{test} \\ Dy'_j &= y_{test} \end{aligned} \quad . \tag{5.3.5}$$

Under these conditions, we calculate the chip thickness using Eq. 5.3.6 for up or down milling with less than or equal to 50% radial immersion or Eq. 5.3.7 for greater than 50% radial immersion.

$$h_j = \sqrt{\left(Cx_j - Dx'_j\right)^2 + \left(Cy_j - Dy'_j\right)^2} \tag{5.3.6}$$

$$h_j = \sqrt{\left(Dx'_j - Dx_j\right)^2 + \left(Dy'_j - Dy_j\right)^2} \tag{5.3.7}$$

In any case that the computed chip thickness is greater than zero, we calculate the tangential and normal force components, $F_{t,j}$ and $F_{n,j}$, respectively, for tooth j according to Eq. 5.3.8, where we have included the edge effects described in Section 4.7:

$$\begin{aligned} F_{t,j} &= k_t b h_j + k_{te} b \\ F_{n,j} &= k_n b h_j + k_{ne} b \end{aligned} \quad , \tag{5.3.8}$$

where k_t and k_n are the force model cutting (shearing) coefficients and k_{te} and k_{ne} are the edge (rubbing/plowing) coefficients. Next, we project the forces $F_{t,j}$ and $F_{n,j}$ onto the x and y directions using Eq. 5.3.9. We then sum the x and y direction forces over all teeth engaged in the cut at the given instant in time, $F_x = \sum_{j=1}^{N_t} F_{x,j}$ and $F_y = \sum_{j=1}^{N_t} F_{y,j}$. We use these force values to determine the instantaneous displacements x_{tool} and y_{tool} for the next time step by numerical integration of the modal equations of motion with the appropriate modal parameters. If multiple vibration modes are included, we sum the displacement contributions from each mode to determine the total displacement. Provided the modal parameters were determined from a direct FRF measurement (or model), we use the same forces for each vibration mode as shown in Section 3.5.

$$\begin{aligned} F_{x,j} &= -F_{t,j} \cos(\phi_j) - F_{n,j} \sin(\phi_j) \\ F_{y,j} &= F_{t,j} \sin(\phi_j) - F_{n,j} \cos(\phi_j) \end{aligned} \tag{5.3.9}$$

In the case of a helical cutting edge, we segment the tool into multiple slices along its axis, each of which is treated as having a zero helix angle. We sum the forces for all slices to determine the total normal and tangential cutting force components for that particular simulation time step (and cutter angular orientation). We then apply Eq. 5.3.9 to project the forces onto the x and y directions, sum the forces over all the teeth engaged in the cut, and complete the numerical integration. The difference, $\Delta\phi$ (deg), between the tooth angle, ϕ_j, for tooth j on slice k and the angle for the same tooth j on slice $k+1$ (located farther away from the tool tip by a distance b/SA) is provided in Eq. 5.3.10, where γ is the helix angle, SA is the number of axial slices, and d is the cutter diameter.

$$\Delta\phi = \frac{2b\tan(\gamma)}{SA \cdot d} \cdot \frac{180}{\pi} \tag{5.3.10}$$

Example 5.3.1: Comparison of time-domain simulation results to Ex. 5.2.2 In order to demonstrate the capabilities of the cycloidal tool path time-domain simulation (p_5_3_1_1.m) described in the previous paragraphs, let's compare results with those obtained from the frequency-domain analysis in Ex. 5.2.2. We'll use the same specifications: 50% radial immersion up milling, $N_t = 4$, $\gamma = 30$ deg, $d = 12.7$ mm diameter, $f_t = 0.1$ mm/tooth, $k_t = 700$ N/mm^2, $k_n = 210$ N/mm^2, $k_{te} = k_{\text{ne}} = 0$ N/mm, and symmetric structural dynamics with a stiffness of 1×10^7 N/m, 1% damping, and 500 Hz natural frequency. The stability lobe diagram for this situation is provided in Fig. 5.2.4. As a first step, we will verify the stability behavior at $\Omega = 6000$ rpm and 7500 rpm for an axial depth of 4 mm. Figure 5.3.3 displays the y direction force and

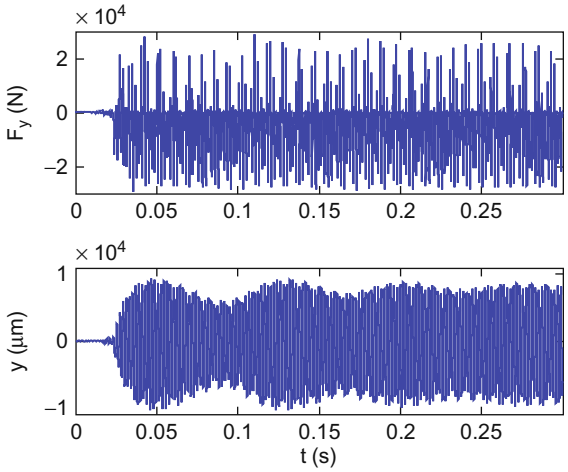

Fig. 5.3.3 Example 5.3.1 y direction force (top) and displacement (bottom) versus time results. Unstable behavior for $\Omega = 6000$ rpm and $b = 4$ mm is observed

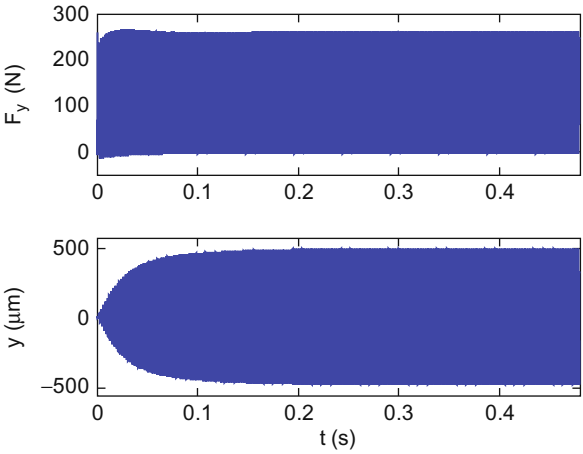

Fig. 5.3.4 Example 5.3.1 y direction force (top) and displacement (bottom) versus time results. Stable behavior for $\Omega = 7500$ rpm and $b = 4$ mm is seen

displacement for 6000 rpm. As expected, the cut is strongly unstable. Figure 5.3.4 shows the stable result for 7500 rpm.

In addition to the time plots, we can also use the simulation to display the x versus y tool path. Figure 5.3.5 presents the results for the $\Omega = 7500$ rpm 50% radial immersion up milling cut with $b = 4$ mm at the tool point, i.e., the axial slice nearest the free end of the tool. Only the portion of the tool path where the teeth enter the material (i.e., the "top" of the tool for the up milling case) is

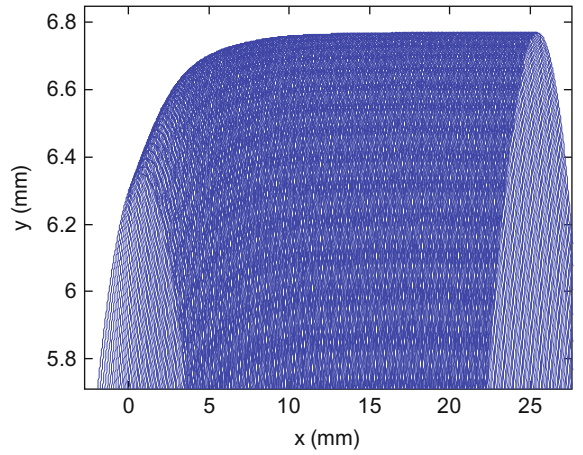

Fig. 5.3.5 Tool path for $\Omega = 7500$ rpm 50% radial immersion up milling cut with $b = 4$ mm. The x versus y teeth coordinates are shown for the axial slice nearest the free end of the cutter

included. The tool center is nominally located at $y = 0$, while the x position varies with the time dependent feed. We can see that the top of the path is initially at the tool radius of 6.35 mm (near $x = 0$). After the entry transients, the y displacement approaches 6.77 mm at the path apex where the machined surface is located. This indicates an overcut condition because more material is removed than commanded for the up milling cut. Note that the material to be cut away is located above the tool in Fig. 5.3.5. Other axial slices can also be selected using the `plot_depth` variable in p_5_3_1_1.m, where a value of one designates the slice at the tool point and larger integer values (up to `steps_axial`) specify slices nearer the spindle face.

The benefit of this figure is that it can be used to isolate the machined surface. Using a trimming algorithm to identify only the extreme points on the tool path, which define the machined surface geometry, the surface location error and roughness average, *Ra* [24], are determined to be 420 μm and 0.2 μm, respectively, from Fig. 5.3.5. The discrete roughness average equation is provided in Eq. 5.3.11, where n is the number of points that define the machined surface. Figure 5.3.6 displays the individual points and surface (solid line that connects the points) for the selected axial slice (`plot_depth = 1`). The small slope in the line indicates that steady state has not quite been reached. However, the (overcut) surface location error value of 420 μm agrees with the tool point frequency-domain solution results previously reported in Fig. 5.2.5 (read the contour value at the coordinates $\Omega = 7500$ rpm and $b = 4$ mm to verify this statement). The surface location error is determined by comparing the y coordinate of the mean of this line to the tool radius (the commanded surface location). For the up milling case shown, if the line is positioned above the tool radius, more material is removed than commanded and an overcut surface is obtained. The trimming algorithm used to identify the machined surface at the selected axial slice proceeds by:

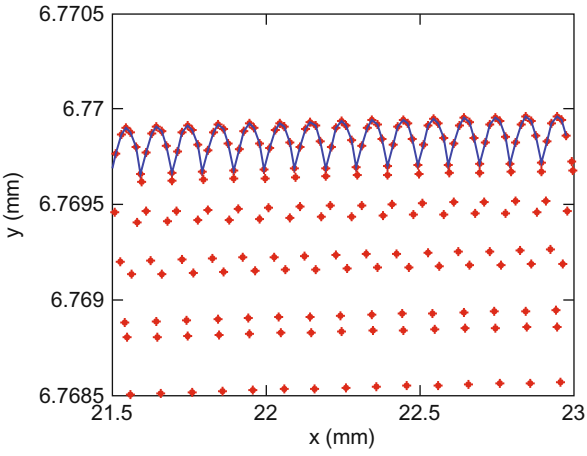

Fig. 5.3.6 The machined surface geometry (line) is defined by isolating the extreme points from the tool path. The surface location error is determined by comparing the mean of this line to the tool radius (the commanded surface location). For the up milling case shown, if the line is positioned above the tool radius, more material is removed than commanded and an overcut surface is obtained

- arranging all points on the tool path in ascending x (feed direction) values;
- selecting a point and comparing its y value to the y values of the next two points;
- keeping the higher point from the next two points for up milling and lower point for down milling;
- incrementing to the next point and repeating the comparison process; and
- repeating the entire exercise multiple times to "bubble up" (up milling) or "trickle down" (down milling) to the final surface.

Although this is not a particularly elegant solution, it is effective. We do not have a defined stopping condition for the procedure, but experience has shown that 50 to 100 iterations are generally adequate.

$$Ra = \frac{\sum_{i=1}^{n} |y_i - \bar{y}|}{n} \tag{5.3.11}$$

Once the surface location error has been determined for all axial slices, the change in error with axial depth can be interrogated as shown in the Section 5.2; see Figs. 5.2.11 and 5.2.12. The time-domain simulation results (circles) are superimposed on the frequency-domain solution (line) in Fig. 5.3.7 for the conditions described in Ex. 5.3.1. For the time-domain solution, five axial slices were used so that $db = 4/5 = 0.8$ mm. The points are placed at the midpoint of each slice in the figure, i.e., {0.4, 1.2, 2, 2.8, and 3.6} mm. The MATLAB® program p_5_3_1_2.m was used to generate the frequency-domain results in Fig. 5.3.7. The time-domain results were obtained from p_5_3_1_1.m by sequentially plotting and trimming the tool path for `plot_depth = 1, 2, ..., 5`.

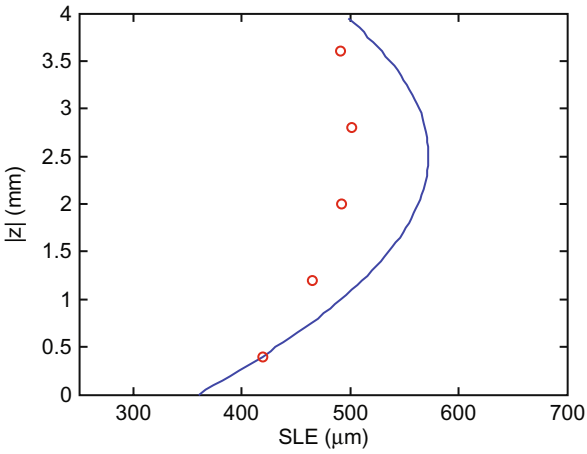

Fig. 5.3.7 Variation in surface location error with axial location. The circles represent the time-domain result for each axial slice; they are located at the midpoint of each of the five slices. The line displays the frequency-domain solution

IN A NUTSHELL As with stability, the use of time-domain simulation to predict surface location error eliminates many of the simplifying assumptions. The tool path may be modeled as a cycloid instead of a circle. Unequal teeth spacing may be applied (see Section 6.3). The surface produced by an unstable cut may be predicted. For the analytical solution, these features are difficult to incorporate. For time-domain simulation, on the other hand, they are relatively easy to include.

Exercises

1. Determine the value of the mean y direction cutting force for the following cuts using Eq. 5.2.3. The aluminum alloy-four tooth cutter combination gives: $k_t = 790$ N/mm^2 and $k_n = 190$ N/mm^2, $k_{te} = 8$ N/mm, and $k_{ne} = 4$ N/mm. Also, $b = 5$ mm and $f_t = 0.15$ mm/tooth. Assume a rigid cutting tool and workpiece.

   a) Up milling, 30% radial immersion
   b) Down milling, 40% radial immersion

2. Plot the y direction force over one cutter revolution for: down milling, 50% radial immersion, $N_t = 2, d = 19$ mm, $\gamma = 30$ deg, $b = 2$ mm, $f_t = 0.2$ mm/tooth, $k_t = 730$ N/mm^2, $k_n = 205$ N/mm^2, $k_{te} = k_{ne} = 0$ N/mm, and $\Omega = 10000$ rpm. Use the Fourier series approach and show results for both five and 25 terms.
3. Calculate the surface location error for the following conditions: 25% radial immersion down milling, spindle speeds from 11000 rpm to 13000 rpm, $N_t = 4, \gamma = 30$ deg, $d = 12.7$ mm diameter, $f_t = 0.15$ mm/tooth, $b = 2$ mm, $k_t = 700$ N/mm^2, $k_n = 210$ N/mm^2, $k_{te} = k_{ne} = 2$ N/mm, and symmetric structural dynamics with a stiffness of 8×10^6 N/m, $\zeta = 0.02$, and 800 Hz natural frequency. For the Fourier computations, use 15 terms, five axial steps, and a spindle speed resolution of 20 rpm. At a spindle speed of 12140 rpm, is the surface overcut or undercut?
4. Using time-domain simulation, determine the surface location error at the free end of the cutter for the same conditions described in Exercise 3. Use a spindle speed equal to the best speed calculated from Eq. 4.3.7 for the $N = 0$ (rightmost) lobe. Carry out your simulation for 40 revolutions with 500 steps per tooth.

References

1. Kline, W., DeVor, R., and Shareef, I., 1982, The Prediction of Surface Accuracy in End Milling, Journal of Engineering for Industry, 104: 272–278.
2. Kline, W., DeVor, R., and Lindberg, J., 1982, The Prediction of Cutting Forces in End Milling with Application to Cornering Cuts, International Journal of Machine Tool Design Research, 22: 7–22.

3. Tlusty, J., 1985, Effect of End Milling Deflections on Accuracy, in: R.I. King (Ed.), Handbook of High Speed Machining Technology, Chapman and Hall, New York, pp. 140–153.
4. Sutherland, J. and DeVor, R., 1986, An Improved Method for Cutting Force and Surface Error Prediction in Flexible End Milling Systems, Journal of Engineering for Industry, 108: 269–279.
5. Montgomery, D. and Altintas, Y., 1991, Mechanism of Cutting Force and Surface Generation in Dynamic Milling, Journal of Engineering for Industry, 113/2: 160–168.
6. Smith, S. and Tlusty, J., 1991, An Overview of Modeling and Simulation of the Milling Process, Journal of Engineering for Industry, 113/2: 169–175.
7. Altintas, Y., Montgomery, D., and Budak, E., 1992, Dynamic Peripheral Milling of Flexible Structures, Journal of Engineering for Industry, 114/2: 137–145.
8. Tarng, Y., Liao, C., and Li, H., 1994, A Mechanistic Model for Prediction of the Dynamics of Cutting Forces in Helical End Milling, International Journal of Modeling and Simulation, 14/2: 92–97.
9. Schmitz, T. and Ziegert, J., 1999, Examination of Surface Location Error Due to Phasing of Cutter Vibrations, Precision Engineering, 23/1: 51–62.
10. Altintas, Y., 2000, Manufacturing Automation, Cambridge University Press, Cambridge, UK.
11. Mann, B., Bayly, P, Davies, M. and Halley, J., 2004, Limit Cycles, Bifurcations, and Accuracy of the Milling Process, Journal of Sound and Vibration, 277: 31–48.
12. Schmitz, T., Couey, J., Marsh, E., Mauntler, N., and Hughes, D., 2007, Runout Effects in Milling: Surface finish, Surface Location Error, and Stability, International Journal of Machine Tools and Manufacture, 47: 841–851.
13. Yun, W.-S., Ko, J., Cho, D.-W., and Ehmann, K., 2002, Development of a Virtual Machining System, Part 2: Prediction and Analysis of a Machined Surface Error, International Journal of Machine Tools and Manufacture, 42: 1607–1615.
14. Tlusty, G., 2000, Manufacturing Equipment and Processes, Prentice-Hall, Upper Saddle River, NJ, Section 9.5.5, Fig. 9.50.
15. Schmitz, T., Ziegert, J., Canning, J.S., and Zapata, R., 2007, Case Study: A Comparison of Error Sources in High-Speed Milling, Precision Engineering, 32: 126–133.
16. Tlusty, J., Zaton, W., and Ismail, F., 1983, Stability Lobes in Milling, Annals of the CIRP, 32/1: 309–313.
17. Altintas, Y. and Budak, E., 1995, Analytical Prediction of Stability Lobes in Milling, Annals of the CIRP, 44/1: 357–362.
18. Schmitz, T. and Mann, B., 2006, Closed Form Solutions for Surface Location Error in Milling, International Journal of Machine Tools and Manufacture, 46: 1369–1377.
19. Ikua, B.W., Tanaka, H., Obata, F., and Sakamoto, S., 2001, Prediction of Cutting Forces and Machining Error in Ball End Milling of Curved Surfaces – I. Theoretical Analysis, Precision Engineering, 25/4: 266–73.
20. Ranganath, S., Narayanan, K., and Sutherland, J., 1999, The Role of Flank Face Interference in Improving the Accuracy of Dynamic Force Predictions in Peripheral Milling, Journal of Manufacturing Science and Engineering, 121: 593–599.
21. Campomanes, M.L. and Altintas, Y., 2003, An Improved Time Domain Simulation for Dynamic Milling at Small Radial Immersions, Journal of Manufacturing Science and Engineering, 125: 416–422.
22. Schmitz, T., Couey, J., Marsh, E., Mauntler, N., and Hughes, D., 2007, Runout Effects in Milling: Surface finish, Surface Location Error, and Stability, International Journal of Machine Tools and Manufacture, 47: 841–851.
23. Chau, W.-M., 1992, Accuracy of Milling Operations Based on Dynamic Models and Simulation, M.S. Thesis, University of Florida.
24. American Society of Mechanical Engineers, 2003, ASME B46.1-2002, Surface Texture (Surface Roughness, Waviness, and Lay), New York, NY.